REGULAR PAPER

Phased Array Radio Navigation System on UAVs: In-Flight Calibration

Mika Okuhara[1] · Torleiv Håland Bryne[1] · Kristoffer Gryte[1] · Tor Arne Johansen[1]

Abstract

Global Navigation Satellite Systems (GNSS) has been the primary positioning solution for Unmanned Aerial Vehicles (UAVs) due to their worldwide coverage, high precision and lightweight receivers. However, GNSS is prone to electromagnetic interference and malicious assaults, including jamming or spoofing because of its low signal-to-noise ratio (SNR). To ensure the continuity and protection of UAV operations, using redundant navigation systems is essential. In recent years, the phased array radio system (PARS) has established itself as a local navigation solution. PARS is robust towards malicious assaults because of an much higher SNR than GNSS regarding directed and encrypted transmission. An essential factor of PARS is that the orientation of the radio antenna at a ground station needs to be precisely determined to obtain the correct positioning of UAVs. This paper presents a method for extending a previously proposed calibration algorithm to estimate the ground antenna orientation with an inertial navigation system (INS) aided by redundant positioning sensors (GNSS, PARS or barometer) using a multiplicative extended Kalman filter (MEKF) so that the calibration can be activated during flights whenever GNSS is available. In other words, the proposed navigation system is essentially an aided-INS which switches between two modes depending on the availability of GNSS: calibration and GNSS aiding mode when GNSS is available (Mode 1) and PARS and barometer aiding mode when GNSS is unavailable (Mode 2). Considering that the navigation system needs to include the effect of Earth's curvature for a long-distance flight, PARS horizontal measurement and the barometer measurement were treated independently, and the navigation equations were propagated in Earth Centred Earth Fixed (ECEF) frame. The independent treatment of barometer measurement, and the propagation in ECEF frame were also beneficial when using multiple ground antennas to have a common reference point and reference frame. The proposed method was validated using data (Inertial Measurement Unit (IMU), GNSS, PARS, Pixhawk autopilot (including barometer) measurements) collected during a field test. In the validation, GNSS was made available at the middle of the flight and the calibration mode was activated for 200s. The proposed navigation system successfully estimated the precise orientation of multiple ground antennas and the navigation solutions were verified using GNSS and Pixhawk autopilot solutions as ground truth.

✉ Mika Okuhara
   mika.okuhara@ntnu.no

   Torleiv Håland Bryne
   torleiv.h.bryne@ntnu.no

   Kristoffer Gryte
   kristoffer.gryte@ntnu.no

   Tor Arne Johansen
   tor.arne.johansen@ntnu.no

[1] Department of Engineering Cybernetics, The Norwegian University of Science and Technology, Trondheim, Norway

1 Introduction

Global Navigation Satellite Systems (GNSS) have been the prime solution for Unmanned Aerial Vehicle (UAV) navigation systems. This solution has some attractive features like global coverage, light receivers, high precision, and low cost. However, due to its low signal-to-noise ratio (SNR), GNSS is prone to natural, unintentional and malicious service interruptions or failures, such as jamming [1] and spoofing [2]. Moreover, a single error could affect the performance or disable the positioning service.

The use of a redundant and GNSS-free positioning solution solves these problems. Thus, establishing a reliable alternative positioning solution to GNSS is becoming

increasingly important for more frequent UAV use, especially for beyond the line of sight (BLOS) flights. In recent years, the phased array radio system (PARS) has proven its potential with small UAVs, [3–6]. Although PARS is primarily used as a high-bandwidth radio communication link, it can also be used for position determination [4]. The heavily encrypted communication built into this system compensates for the lack of security in commercially available GNSS solutions by a much higher SNR. However, the downside of PARS is that it requires a radio link and is less accurate than standard GNSS solutions, [3–6].

In terms of cybersecurity and the need for a GNSS-free solution, PARS as a navigation system for small UAVs has been a subject of continuous research for several years. In an earlier phase of the previous work, a non-linear observer was used for the PARS-aided inertial navigation system (INS) [4], and spoofing detection and mitigation in combination with GNSS- and PARS-aided INS [5]. In more recent work, PARS-aided INS was implemented using the Multiplicative Extended Kalman Filter (MEKF) [7, 8]. The method was changed to MEKF as it can couple estimation errors between all states and make use of the cross-covariance between states when fusing inertial and PARS measurements [6, 9]. Although the precise estimate of the ground antenna orientation was necessary for accurate positioning in PARS, in previous work, this was done manually, either by measuring position and attitude with a GNSS receiver and compass or by manually aligning PARS with the GNSS position in a post-process analysis. Thus, in the most recent work, an automatic calibration algorithm to precisely estimate the full pose of a PARS ground antenna was implemented, also using MEKF [10].

1.1 Main Contributions

The main idea of this paper is to enhance the calibration algorithm developed in [10]. The major improvements are the following:

- The standalone calibration algorithm was integrated with the MEKF-based aided-INS such that we can perform the calibration online whenever GNSS measurements are available during flights. Previous research has only considered offline calibration.
- The algorithm integrated with the aided-INS enabled it to estimate the full poses of *multiple* PARS ground radios. We achieved this by including the ground antennas' orientation and their kinematics in the extended state vector and the matrices of the MEKF.
- Further improvements to the entire aided-INS system were also made:

- The navigation equations were propagated in ECEF frame instead of NED frame, unlike the previous work [4–6, 9]. Using the ECEF frame as the navigation frame eases the calibration of multiple ground antennas by having a common reference frame. It also improves the use of PARS-aided INS in long-duration flight since this formulation considers the curvature of the Earth, and the navigation system directly outputs an unambiguous global position estimate.
- Moreover, this article also takes advantage of a direct barometer measurement providing vertical aiding to the INS as in [4, 5]. However, the barometer measurement was treated independently from PARS measurements, unlike [4, 5], to consider the curvature of the Earth, and to have an altitude reference point independent of any ground antennas not considered in previous works.

This method enables online refinement of the PARS-based navigation accuracy during a flight, even in the situation of GNSS unavailability at the initial stage of flight. Furthermore, considering that the calibration accuracy benefits from a long calibration period and a long-range between the UAV and the ground station, it gives a large extent of flexibility. To validate the proposed method, we conducted a field test using a fixed-wing UAV with IMU and Pixhawk autopilot (including barometer) onboard, GNSS receiver and *two* PARS ground antennas to collect sensor measurements from a real flight and performed offline calculations using the data. The navigation solutions from the offline calculations were verified using GNSS measurement and Pixhawk autopilot solution as reference.

1.2 Organization

This paper starts with mathematical preliminaries in Section 2. Brief concepts of positioning techniques are described in Section 3. Section 4 presents the basics of MEKF-based navigation system using multiple sensor measurements and explains how the calibration algorithm runs along with it. Practical aspects of a test flight are then described in Section 5 and the results from the navigation system with calibration are discussed in Section 6.

2 Preliminaries

Before presenting the positioning techniques and the MEKF-based navigation system, some mathematical preliminaries are presented in this section.

2.1 Notation

The Euclidean vector norm is denoted $\| \cdot \|_2$, and the $n \times n$ identity matrix is denoted $\boldsymbol{I}_n$. The transpose of a vector or a matrix is denoted $(\cdot)^{\mathsf{T}}$. Coordinate frames are expressed as $\{\cdot\}$, while $z_{bc}^a \in \mathbb{R}^3$ denotes a vector z from frame $\{b\}$ to $\{c\}$, resolved in $\{a\}$. $\boldsymbol{S}(\cdot) \in SS(3)$ denotes a skew symmetric matrix such that $\boldsymbol{S}(z_1)z_2 = z_1 \times z_2$, and $z_1 \cdot z_2$ is a dot product for the two vectors $z_1, z_2 \in \mathbb{R}^3$. In addition, $\mathrm{diag}(\star_1, ..., \star_n)$ represents a diagonal matrix which places the n arguments diagonally, and error variables are represented with with $\delta\star$, where $\star$ is a variable placeholder.

2.2 Attitude Representations and Relationships

The rotation vector

$$\boldsymbol{a}_\phi \equiv \phi\boldsymbol{e} \tag{1}$$

is a general class of three-parameter attitude representations of a rigid body with one point fixed whose rotation is denoted by the angle ϕ about some axis, which we specify by a unit vector $\boldsymbol{e}$.

In this paper, attitudes are represented as unit quaternions, using the Hamiltonian representation. For a rotation from some frame $\{a\}$ to another frame $\{b\}$, the unit quaternion is given as

$$\boldsymbol{q}_a^b = \begin{pmatrix} q_s \\ \boldsymbol{q}_v \end{pmatrix} = \begin{pmatrix} \cos(\frac{\phi}{2}) \\ \boldsymbol{e}\,\sin(\frac{\phi}{2}) \end{pmatrix}. \tag{2}$$

The unit quaternion contains the *real* or *scalar* part referred as q_s, and the *imaginary* or *vector* part as $\boldsymbol{q}_v = (q_x, q_y, q_z)^{\mathsf{T}}$. The rotation matrix, $\boldsymbol{R}_{ba} \in SO(3)$, represents the rotation between $\{a\}$ and $\{b\}$ frames. The quaternion can be used to calculate the rotation matrix, $\boldsymbol{R}_{ba} \in SO(3)$,

$$\boldsymbol{R}_{ba}(\boldsymbol{q}_a^b) = \left(q_s^2 - \boldsymbol{q}_v^{\mathsf{T}}\boldsymbol{q}_v\right)\boldsymbol{I}_3 + 2q_s\boldsymbol{S}(\boldsymbol{q}_v) + 2\boldsymbol{q}_v\boldsymbol{q}_v^{\mathsf{T}}, \tag{3}$$

as in e.g. [8, Eq. (4)], [7, Eq. (117)] and [11, App. D.2]. The Hamiltonian quaternion product, denoted $\otimes$, is given such that

$$\boldsymbol{q}_3 = \boldsymbol{q}_1 \otimes \boldsymbol{q}_2 = \begin{pmatrix} q_{1_s}q_{2_s} - \boldsymbol{q}_{1_v}^{\mathsf{T}}\boldsymbol{q}_{2_v} \\ q_{1_s}\boldsymbol{q}_{2_v} + q_{2_s}\boldsymbol{q}_{1_v} + \boldsymbol{S}\left(\boldsymbol{q}_{1_v}\right)\boldsymbol{q}_{2_v} \end{pmatrix}, \tag{4}$$

as in [7, Eq. (13)] and [11, App. D.2].

In this paper, the attitude error is denoted $\delta\boldsymbol{q}$ and relates to the true quaternion $\boldsymbol{q}$ by

$$\boldsymbol{q} = \hat{\boldsymbol{q}} \otimes \delta\boldsymbol{q}(\delta\boldsymbol{a}) \tag{5}$$

where $\hat{\boldsymbol{q}}$ is the nominal estimated unit quaternion. The three dimensional attitude error in the state of the MEKF, $\delta\boldsymbol{a}$ is parameterized using four times the Modified Rodrigues Parameters (MRPs), $\delta\boldsymbol{a}_{\mathrm{mrp}}$, where

$$\delta\boldsymbol{a}_{\mathrm{mrp}} \equiv \frac{\delta\boldsymbol{q}_v}{1 + \delta q_s} = \boldsymbol{e}\,\tan\left(\frac{\phi}{4}\right) \equiv \frac{\delta\boldsymbol{a}}{4}, \tag{6}$$

as given in [8, Eq. (10)]. The last two terms ensure that $a_p = \|\delta\boldsymbol{a}\|_2$ is approximately equal to ϕ for small rotations. As given in [8, Eq. (18c)], the error quaternion is calculated as

$$\delta\boldsymbol{q}(\delta\boldsymbol{a}) = \frac{1}{16 + a_p^2}\begin{pmatrix} 16 - a_p^2 \\ 8\delta\boldsymbol{a} \end{pmatrix}. \tag{7}$$

Moreover, the kinematic equation of a unit quaternion $\boldsymbol{q}_c^b$ can be given as

$$\dot{\boldsymbol{q}}_c^b = \frac{1}{2}\boldsymbol{q}_c^b \otimes \bar{\boldsymbol{\omega}}_{ac}^c - \frac{1}{2}\bar{\boldsymbol{\omega}}_{ab}^b \otimes \boldsymbol{q}_c^b = \frac{1}{2}\boldsymbol{\Omega}(\boldsymbol{\omega}_{ac}^c)\boldsymbol{q}_c^b - \frac{1}{2}\boldsymbol{\Gamma}(\boldsymbol{\omega}_{ab}^b)\boldsymbol{q}_c^b \tag{8}$$

where $\bar{\boldsymbol{\omega}}_\bullet^\bullet = (0, (\boldsymbol{\omega}_\bullet^\bullet)^{\mathsf{T}})^{\mathsf{T}}$ and ω is an angular velocity vector. Moreover,

$$\boldsymbol{\Omega}(\boldsymbol{\omega}) = \begin{pmatrix} 0 & -\boldsymbol{\omega}^{\mathsf{T}} \\ \boldsymbol{\omega} & -\boldsymbol{S}(\boldsymbol{\omega}) \end{pmatrix}, \quad \boldsymbol{\Gamma}(\boldsymbol{\omega}) = \begin{pmatrix} 0 & -\boldsymbol{\omega}^{\mathsf{T}} \\ \boldsymbol{\omega} & \boldsymbol{S}(\boldsymbol{\omega}) \end{pmatrix}. \tag{9}$$

Additionally, the Euler angles (roll, pitch and yaw) are represented as

$$\boldsymbol{\Theta} = \left(\phi, \theta, \psi\right)^{\mathsf{T}}, \tag{10}$$

and relate to rotation matrix using

$$\boldsymbol{R}(\Theta) = \begin{pmatrix} c\theta c\psi & -c\phi s\psi + s\phi s\theta c\psi & s\phi s\psi + c\phi s\theta c\psi \\ c\theta s\psi & c\phi c\psi + s\phi s\theta s\psi & -s\phi c\psi + c\phi s\theta s\psi \\ -s\theta & s\phi c\theta & c\phi c\theta \end{pmatrix} \tag{11}$$

where $c\star$ denotes $\cos(\star)$ and $s\star$ denotes $\sin(\star)$.

2.3 Coordinate Frames

This paper considers $4 + 2m$ coordinate frames. The first four are the Earth centered Inertial (ECI) frame, the Earth Centered Earth Fixed (ECEF) frame, the North East Down (NED) frame and the BODY reference frame of the UAV, denoted $\{i\}$, $\{e\}$, $\{n\}$ and $\{b\}$ respectively, as indicated in Fig. 1. Please note that this paper resolves navigation equations in the $\{e\}$-frame, while the previous work [6, 9] uses a Earth-fixed $\{n\}$-frame instead.
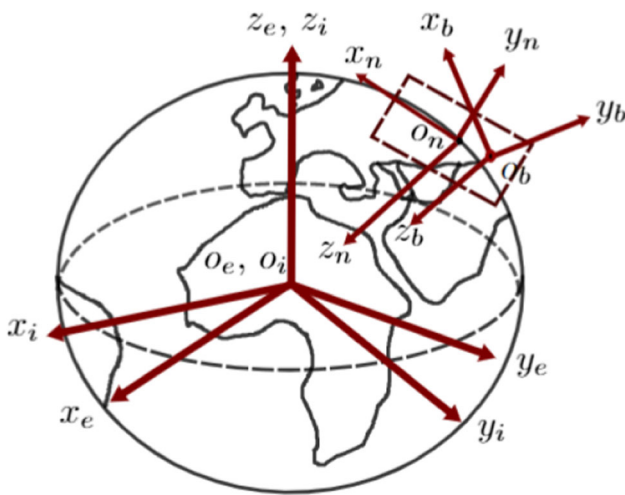
Fig. 1 Definitions of the ECI, the ECEF, the NED and the BODY coordinate frames

Fig. 2 Range/azimuth/elevation measurements in PARS. ψ_r denotes the yaw angle between $\{n_j\}$ and $\{r_j\}$[1]

The remaining $2m$ coordinate frames are the local PARS coordinate frames and the local NED frames, denoted $\{r_j\}$ and $\{n_j\}$, where j is the PARS index and m is the number of PARS ground antennas in use. The PARS coordinate system resembles the local NED frame with coincided origins (i.e. $O_{n_j} = O_{r_j}$), however, rotated with respect to the NED frame to be aligned with the PARS ground antennas, as indicated in Fig. 2. Please note that the origin of the $\{n_j\}$-frame is located in the center of the respective PARS ground radio antenna, while the origin of the $\{n\}$-frame follows the UAV. Thus totaling $1 + m$ NED frames.

3 Positioning

This section describes the positioning techniques used in the MEKF-based navigation system.

3.1 Real-time Kinematic GNSS

Real-time kinematic positioning (RTK) is known as high-precision GNSS. By performing a relative position determination from a GNSS base station with a known position to a rover by transmitting raw GNSS observable from the ground station to the rover (UAV in this work), RTK can achieve centimetre accuracy. The RTK GNSS solution was used in this work due to its high precision to provide the ground truth of the UAV position, $\boldsymbol{p}_{eb}^e \in \mathbb{R}^3$.

3.2 Phased Array Radio System positioning

Although PARS' primary usage is communication, it can also be used as a positioning system as stated earlier. Basic principles are similar to those in [12, Ch. 13.3.4].
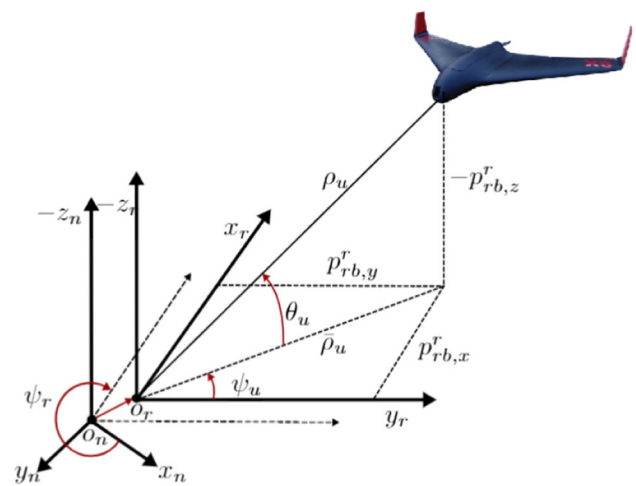
The azimuth angle ψ_u and elevation angle θ_u of the UAV in the PARS coordinate frame $\{r\}$ can be measured from the phase difference in the incoming signals between the elements of the terrestrial radio antenna [1]. This is known as the direction of arrival (DoA) problem [13–15]. By precisely timing the signal transmission time, a geometric range ρ_u between the PARS ground antenna and the UAV is found. A physical intuition of the range ρ_u, elevation angle θ_u and azimuth angle ψ_u in frame $\{r\}$ can be seen in Fig. 2. Including zero-mean Gaussian noise $\varepsilon_\star \sim \mathcal{N}(0, \sigma_\star^2)$, the actual measurements are represented as

$$\rho_y = \rho_u + \varepsilon_\rho, \tag{12}$$

$$\psi_y = \psi_u + \varepsilon_\psi, \tag{13}$$

$$\theta_y = \theta_u + \varepsilon_\theta. \tag{14}$$

The range ρ_u, azimuth ψ_u and elevation θ_u can be related to the Cartesian UAV position in the $\{r\}$-frame using

$$\boldsymbol{p}_{\text{PARS}}^r = \begin{pmatrix} p_{rb,x}^r \\ p_{rb,y}^r \\ p_{rb,z}^r \end{pmatrix} = \begin{pmatrix} \rho_u \cos(\psi_u) \cos(\theta_u) \\ \rho_u \sin(\psi_u) \cos(\theta_u) \\ -\rho_u \sin(\theta_u)) \end{pmatrix}, \tag{15}$$

which is derivable from Fig. 2.

The PARS position can be converted from the $\{r\}$-frame to the $\{n\}$-frame using

$$\boldsymbol{p}_{\text{PARS}}^n = \boldsymbol{R}_{nr}(\boldsymbol{q}_r^n) \boldsymbol{p}_{\text{PARS}}^r \tag{16}$$

where the unit quaternion $\boldsymbol{q}_r^n$ represents the rotation from $\{r\}$ to $\{n\}$, which is obtained during the calibration of the mounting of the PARS ground antenna.

---

[1] The index j is omitted in this section for convenience.

3.3 Inertial Navigation System

INS is an example of a dead-reckoning navigation system, whose position is maintained by integrating acceleration and angular rate measurements obtained using an inertial measurement unit (IMU) [16, Ch. 5].

3.3.1 Inertial Measurement Unit

A simplified measurement model of IMU, providing specific force (f^b_{IMU}) and angular rate sensor (ARS) measurements (ω^b_{IMU}) is given as

$$f^b_{\text{IMU}} = f^b_{ib} + b^b_{acc} + \varepsilon^b_{acc} \tag{17}$$

$$\omega^b_{\text{IMU}} = \omega^b_{ib} + b^b_{ars} + \varepsilon^b_{ars} \tag{18}$$

where $b^b_\star$ is the accelerometer (ACC) and the ARS biases, and $\varepsilon^b_\star$ is zero-mean noise. The biases are modeled as Gauss-Markov processes

$$\dot{b}^b_\star = -T^{-1}_\star b^b_\star + \varepsilon_{b_\star} \tag{19}$$

where $\varepsilon_{b_\star}$ assumed to be is zero-mean white noise, and $T_\star$ represents the time constant matrices of the two processes.

3.3.2 Strapdown Equations

The position and velocity of the UAV with respect to the $\{e\}$-frame are denoted as $p^e_{eb} \in \mathbb{R}^3$ and $v^e_{eb} \in \mathbb{R}^3$. The attitude and the angular rate of the UAV relative to the $\{e\}$-frame are given as the unit quaternion q^e_b and as $\omega^b_{eb} = \omega^b_{ib} - R^{\mathsf{T}}_{eb}\omega^e_{ie} \in \mathbb{R}^3$. The gravity vector is given as $g^e_b(p^e_{eb})$ and can be calculated using [16, Ch. 2.4.7]. The strapdown equation results in

$$\dot{p}^e_{eb} = v^e_{eb} \tag{20}$$

$$\dot{v}^e_{eb} = -2S(\omega^e_{ie})v^e_{eb} + R_{eb}f^b_{ib} + g^e_b \tag{21}$$

$$\dot{q}^e_b = \frac{1}{2}\Omega(\omega^b_{ib})q^e_b - \frac{1}{2}\Gamma(\omega^e_{ie})q^e_b \tag{22}$$

where $\omega^e_{ie} = (0, 0, \omega_{ie})^{\mathsf{T}}$ is the angular rate of the Earth rotation.

4 Navigation System

The navigation system proposed in this paper is essentially an aided-INS. Figure 3 illustrates the overview of the navigation system. The system dynamics is propagated using IMU measurements (i.e. INS), and MEKF applies corrections to the INS-based system dynamics [17]. Fundamentally, the INS was aided in two modes: The first mode is GNSS and PARS-aided INS such that the calibration algorithm [10] runs simultaneously to estimate the PARS ground antenna orientations, and the second mode is PARS and barometer-aided INS. The navigation system switches between the two modes depending on the availability of GNSS measurements. In Fig. 3, the decision block 'GNSS' determines the mode. If no measurement is available in the second mode, the INS is propagated without any aid, as the process block 'No Aid' indicates.

The main feature of MEKF is that it estimates the error between nominal state and true state instead of estimating a full state. The error state δx is estimated as a correction to the nominal state estimate $\hat{x}$ to get closer to the true state x:

$$x = \hat{x} \otimes \delta x. \tag{23}$$

Here, the $\oplus$ operator represents the + or the $\otimes$ operator (Hamiltonian quaternion product) depending on the state. Please note that the system dynamics was propagated in $\{e\}$-frame instead of $\{n\}$-frame, and the barometer-based altitude was treated separately from PARS measurements, unlike the previous work [3–6, 9]. These changes were made to include the effect of the Earth curvature.

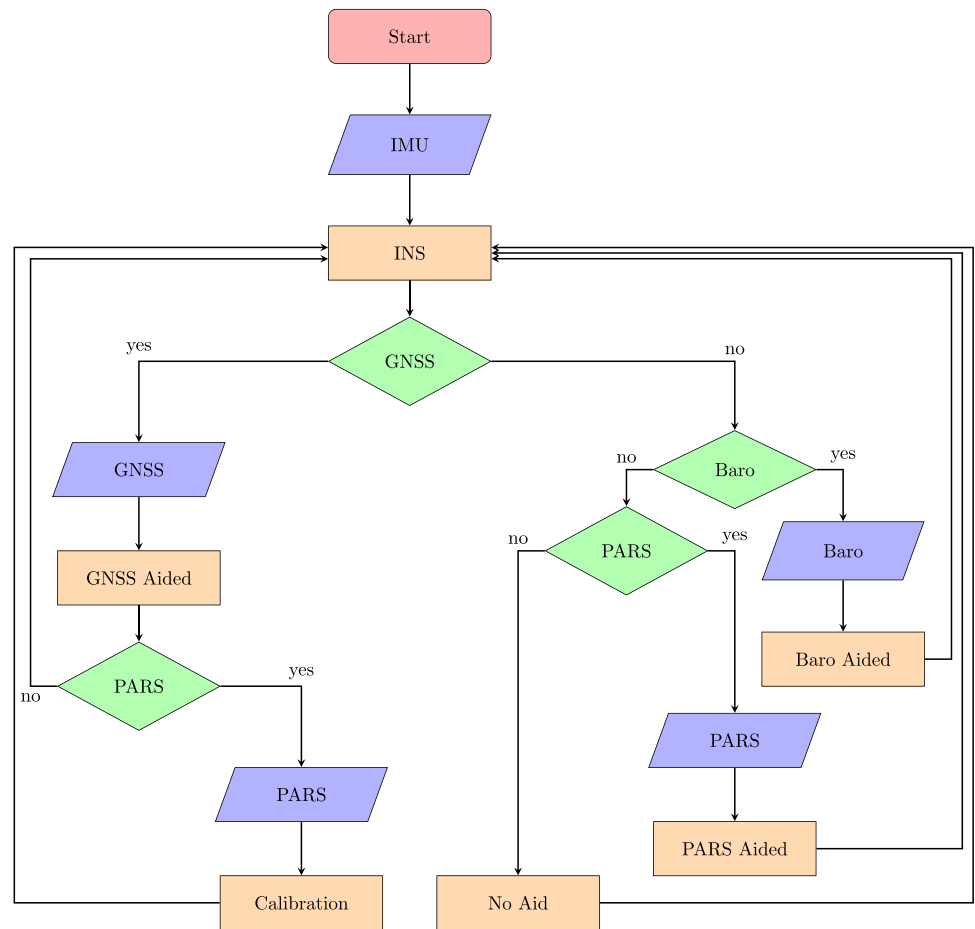### 4.1 Navigation System Model

4.1.1 Nominal System Kinematics

The nominal state estimate (i.e. the state vector of the INS) was given as

$$\hat{x} = (\hat{p}^e_{eb}, \ \hat{v}^e_{eb}, \ \hat{q}^e_b, \ \hat{b}^b_{\text{acc}}, \ \hat{b}^b_{\text{ars}}, \ q^{n_1}_{r_1}, \ \ldots, \ q^{n_m}_{r_m})^{\mathsf{T}} \in \mathbb{R}^{16+4m}, \tag{24}$$

where $q^{n_j}_{r_j}$ is the PARS ground antenna orientation, which is essentially the relative orientation of the PARS coordinate frame $\{r_j\}$ and the navigation frame $\{n_j\}$ for ground antenna $j \in [1, m]$.

The nominal state is updated using the following kinematic model based on the strapdown equations presented in

Fig. 3 Flowchart of the navigation system

Section 3.3:

$$\dot{\hat{p}}^e_{eb} = \hat{v}^e_{eb} \tag{25a}$$

$$\dot{\hat{v}}^e_{eb} = -2S(\omega^e_{ie})\hat{v}^e_{eb} + \hat{R}_{eb}\hat{f}^b_{ib} + g^e_b(\hat{p}^e_{eb}) \tag{25b}$$

$$\dot{q}^e_b = \frac{1}{2}\Omega(\hat{\omega}^b_{ib})q^e_b - \frac{1}{2}\Gamma(\omega^e_{ie})q^e_b \tag{25c}$$

$$\dot{\hat{b}}^b_{acc} = -T^{-1}_{acc}\hat{b}^b_{acc} \tag{25d}$$

$$\dot{\hat{b}}^b_{ars} = -T^{-1}_{ars}\hat{b}^b_{ars} \tag{25e}$$

$$\dot{\hat{q}}^{n_1}_{r_1} = 0 \tag{25f}$$

$$\vdots$$

$$\dot{\hat{q}}^{n_m}_{r_m} = 0 \tag{25g}$$

$$\hat{f}^b_{ib} = f^b_{IMU} - \hat{b}^b_{acc} \tag{25h}$$

$$\hat{\omega}^b_{ib} = \omega^b_{IMU} - \hat{b}^b_{ars}, \tag{25i}$$

The derivatives of $q^{n_j}_{r_j}$ are zero, as the ground antennas are stationary. The Eq. (25) can be computed in discrete time using any integration methods. Exact integration methods concerting the quaternion integration can be found in [11].

4.1.2 Error-State System Kinematics

The error state (i.e. the state vector of the MEKF) was given as

$$\delta x = (\delta p^e_{eb}, \ \delta v^e_{eb}, \ \delta a^e_b, \ \delta b^b_{acc}, \ \delta b^b_{ars}, \ \delta a^{n_1}_{r_1}, \ \dots \delta a^{n_m}_{r_m})^\mathsf{T}$$
$$\in \mathbb{R}^{15+3m}. \tag{26}$$

Please note that the 3D attitude error states $\delta a^\star_\star$ (UAV and ground radio) paramatrized as four times MRPs rather than rotation matrices or quaternions, are used to update the INS's states when correcting the nominal state using Eqs. 5 and 7.

The continuous-time linearized error state system model is

$$\delta \dot{x} = F(t)\delta x + G(t)w, \tag{27}$$

where $w = (\varepsilon^\mathsf{T}_{acc}, \varepsilon^\mathsf{T}_{ars}, \varepsilon^\mathsf{T}_{b_{acc}}, \varepsilon^\mathsf{T}_{b_{ars}}, \varepsilon^\mathsf{T}_{\delta a_1}, \dots, \varepsilon^\mathsf{T}_{\delta a_m})^\mathsf{T}$ is the process noise with spectral density $\mathcal{Q}$ given by $\mathbb{E}[w(t)w^\mathsf{T}(\tau)] = \mathcal{Q}\delta(t-\tau) \in \mathbb{R}^{(12+3m)\times(12+3m)}$. The Jacobian matrices F and G, and the spectral density matrix $\mathcal{Q}$ are given in Appendix A.

4.2 Measurement Model, Mode 1: PARS Calibration (GNSS Available)

When GNSS measurements are available, the navigation system uses GNSS to aid the INS while running the calibration of PARS ground antenna mounting presented in [10] simultaneously.

4.2.1 GNSS

The GNSS measures the position of the UAV in the $\{e\}$-frame, therefore

$$y_{\text{gnss}}^e = \hat{p}_{eb}^e + \delta p + \varepsilon_{\text{gnss}} \tag{28}$$

$$\Rightarrow \hat{y}_{\text{gnss}}^e = \hat{p}_{eb}^e \tag{29}$$

such that a linear measurement matrix

$$H_{\text{gnss}} = \left(I_3 \; \mathbf{0}_{3\times12} \; \mathbf{0}_{3\times3m} \right) \in \mathbb{R}^{3\times(15+3m)} \tag{30}$$

can be applied in the MEKF. The measurement covariance matrix is given as

$$\mathcal{R}_{\text{gnss}}^e = R_{en} \text{diag}(\mathbb{E}[\varepsilon_{\text{gnss},x}^2], \mathbb{E}[\varepsilon_{\text{gnss},y}^2], \mathbb{E}[\varepsilon_{\text{gnss},z}^2]) R_{en}^\mathsf{T}, \tag{31}$$

where $\varepsilon_{\text{gnss}}$ is zero-mean Gaussian white noise.

4.2.2 PARS: Calibration

To mitigate the noise in the PARS elevation angle, the vertical measurement in Eq. 15 was replaced by utilizing an exogenous altitude measurement:[2]

$$\gamma_{\text{alt}_j} = p_{n_j b, z}^{n_j} + \varepsilon_{\text{alt}_j}. \tag{32}$$

Here, $p_{n_j b, z}^{n_j}$ and γ_{alt_j} relate to the UAV position p_{eb}^e and the respective ground radio $p_{er_j}^e$ in the following manner

$$\gamma_{\text{alt}_j} = (0\ 0\ 1)\, R_{en_j}^\mathsf{T} (p_{eb}^e - p_{er_j}^e) + \varepsilon_{\text{alt}_j}. \tag{33}$$

This arrangement in the vertical measurement is due to the need to have PARS and GNSS-based positions in the calibration algorithm simultaneously. The PARS range was also arranged in a different manner from the Section 4.3 to compute the measurement of the horizontal range:

$$\bar{\rho}_{y_j} = \sqrt{\rho_{y_j}^2 - \gamma_{\text{alt}_j}^2}. \tag{34}$$

---

[2] $p_{r_j b}^{n_j} = p_{n_j b}^{n_j}$ since the origins of $\{n_j\}$ frame and $\{r_j\}$ coincide.

Based on this, the resulting Cartesian position measurement becomes

$$p_{\text{PARS, alt}}^{r_j} = \begin{pmatrix} \bar{\rho}_{y_j} \cos(\psi_{y_j}) \\ \bar{\rho}_{y_j} \sin(\psi_{y_j}) \\ \gamma_{\text{alt}_j} \end{pmatrix}. \tag{35}$$

The measurement model is formulated based on the following relationship between the UAV position (p_{eb}^e), the ground station position ($p_{er_j}^e$) and UAV PARS position relative to the ground radio ($p_{r_j b}^{r_j}$):

$$p_{eb}^e = p_{er_j}^e + R_{en_j} R_{n_j r_j} p_{r_j b}^{r_j}. \tag{36}$$

By arranging Eq. 36 as shown in [10], the equation results in the form suitable for calibration,

$$\underbrace{\hat{R}_{n_j r_j} p_{r_j b}^{r_j}}_{y_{\text{pars}_j}} = \underbrace{R_{en_j}^\mathsf{T} \left(\hat{p}_{eb}^e - p_{er_j}^e \right)}_{\hat{y}_{\text{pars}_j}} + \underbrace{R_{en_j}^\mathsf{T}}_{H_{\text{pos}_j}} \delta p$$

$$+ \underbrace{\hat{R}_{n_j r_j} S\left(p_{r_j b}^{r_j} \right)}_{H_{\text{calib}_j}} \delta a_{r_j}^{n_j} \tag{37}$$

where the measurement, the measurement estimate, and the measurement matrices are respectively

$$y_{\text{pars}_j}^n = \hat{R}_{n_j r_j} p_{\text{PARS, alt}}^{r_j}, \tag{38}$$

$$\hat{y}_{\text{pars}_j}^n = R_{en_j}^\mathsf{T} \left(\hat{p}_{eb}^e - p_{er_j}^e \right), \tag{39}$$

$$H_{\text{pos}_j} = R_{en_j}^\mathsf{T}, \tag{40}$$

$$H_{\text{calib}_j} = \hat{R}_{n_j r_j} S\left(\hat{R}_{er_j}^\mathsf{T} \left(\hat{p}_{eb}^e - p_{er_j}^e \right) \right). \tag{41}$$

The resulting measurement matrix becomes

$$H_{Calib_j}\ \mathbf{0}_{3\times3}).H_{\text{pars}}$$

$$= \begin{pmatrix} H_{\text{pos}_1} & \mathbf{0}_{3\times12} & H_{\text{calib}_1} & & & \mathbf{0}_{3\times3(m-1)} \\ \vdots & \vdots & & \ddots & & \vdots \\ H_{\text{pos}_j} & \mathbf{0}_{3\times12} & \mathbf{0}_{3\times3(j-1)} & H_{\text{calib}_j} & \mathbf{0}_{3\times3(m-j-1)} \\ \vdots & \vdots & & & \ddots & \\ H_{\text{pos}_m} & \mathbf{0}_{3\times12} & & \mathbf{0}_{3\times3(m-1)} & & H_{\text{calib}_m} \end{pmatrix}$$

$$\in \mathbb{R}^{3m\times(15+3m)}. \tag{42}$$

The intermediate calculation between Eqs. 36 and 37 can be found in Appendix B. The position estimate from GNSS-aided INS and the PARS measurement correspond to p_{eb}^e and $p_{r_j b}^{r_j}$ (i.e. $p_{\text{PARS, alt}}^{r_j}$), respectively. $R_{en_j}^\mathsf{T}$ and $p_{er_j}^e$ are considered to be known since these can be computed from the surveyed ground station antenna locations.

Furthermore, the covariance of the original PARS measurement ρ_{y_j}, ψ_{y_j} and γ_{alt_j} is

$$\mathcal{R}_{\text{PARS, alt}} = \text{diag}(\mathbb{E}[\varepsilon_\rho^2], \mathbb{E}[\varepsilon_\psi^2], \mathbb{E}[\varepsilon_{\text{alt}}^2]), \tag{43}$$

and the covariance of $p_{\text{PARS,alt}}^{r_j}$ can be computed using

$$\mathcal{R}_{\text{PARS,alt}}^{r_j} = M_{\text{PARS,alt}} \mathcal{R}_{\text{PARS,alt}} M_{\text{PARS,alt}}^\mathsf{T}. \tag{44}$$

Here, $\mathcal{R}_{\text{PARS,alt}}$ given in cylindrical coordinates is converted to $\mathcal{R}_{\text{PARS,alt}}^{r_j}$ in Cartesian coordinates [18, Ch. 1.6]. $M_{\text{PARS,alt}}$ was computed similarly with Section 4.3. Reference [10] provides further details about computation of $M_{\text{PARS,alt}}$.

$$\mathcal{R}_{\text{PARS,alt}}^{n_j} = R_{n_j r_j} M_{\text{PARS,alt}} \mathcal{R}_{\text{PARS,alt}} M_{\text{PARS,alt}}^\mathsf{T} R_{n_j r_j}^\mathsf{T}, \tag{45}$$

in order to use Eqs. 38–42 in the measurement update.

4.3 Measurement Model, Mode 2: PARS and Barometer (GNSS Unavailable)

As presented in [3], the PARS vertical measurement can be very noisy as the elevation angle is prone to multipath errors due to the reflections from water surfaces. To avoid this issue, the vertical measurement in Eq. 15 was replaced by an altitude measurement based on barometer in [5]. However, as the barometer measures the altitude from the reference surface perpendicular to the tangent line of the Earth curvature, using the barometer altitude directly in the local NED frame induces errors when the flight distance of the UAV becomes longer since this formulation does not take into account the curvature of the Earth. Therefore, in this paper, the barometer altitude as replacement of PARS vertical component was treated separately from the PARS measurements to include the curvature of the Earth.

4.3.1 PARS

A measurement of the horizontal range ($\bar{\rho}_{y_j}$) was computed by approximating the elevation angle (α_j) using a trigonometric relation as shown in Fig. 4:

$$\bar{\rho}_{y_j} = \rho_{y_j} \cos \alpha_j \tag{46}$$

where

$$\cos \alpha_j = \frac{p_{eb}^e \cdot p_{er_j}^e}{\|p_{eb}^e\|_2 \|p_{er_j}^e\|_2}. \tag{47}$$
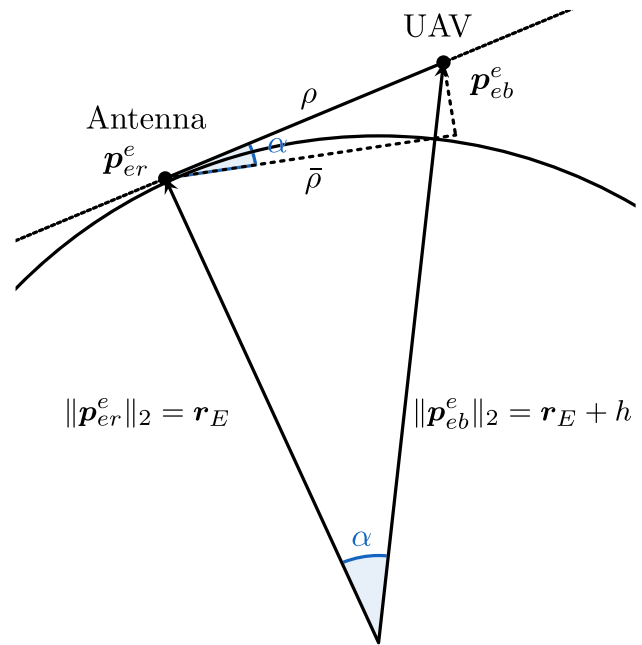

Fig. 4 Approximation of the elevation angle. r_E and h are the Earth radius and a height from the earth surface

The horizontal components of Cartesian PARS position measurements can be expressed as

$$\begin{aligned} y_{\text{PARS}}^{r_j} &= \begin{pmatrix} \bar{\rho}_{y_j} \cos \psi_{y_j} \\ \bar{\rho}_{y_j} \sin \psi_{y_j} \end{pmatrix} \\ &= \begin{pmatrix} 1 & 0 & 0 \\ 0 & 1 & 0 \end{pmatrix} R_{n_j r_j}^\mathsf{T} R_{en_j}^\mathsf{T} \left(p_{eb}^e - p_{er_j}^e \right). \end{aligned} \tag{48}$$

By using the relation $p_{eb}^e = \hat{p}_{eb}^e + \delta p_{eb}^e$, the estimate measurement is given as

$$\hat{y}_{\text{PARS}}^{r_j} = \begin{pmatrix} 1 & 0 & 0 \\ 0 & 1 & 0 \end{pmatrix} \hat{R}_{n_j r_j}^\mathsf{T} R_{en_j}^\mathsf{T} \left(\hat{p}_{eb}^e - p_{er_j}^e \right), \tag{49}$$

while the Jacobian matrix of $y_{\text{PARS}}^{r_j}$ with respect to δp_{eb}^e can be found by differentiating Eq. 49

$$\left. \frac{\partial y_{\text{PARS}}^{r_j}}{\partial \delta p_{eb}^e} \right|_{\delta p_{eb}^e = 0_{3\times 1}} = \underbrace{\begin{pmatrix} 1 & 0 & 0 \\ 0 & 1 & 0 \end{pmatrix}}_{\Pi} \underbrace{\hat{R}_{n_j r_j}^\mathsf{T} R_{en_j}^\mathsf{T}}_{\hat{R}_{er_j}^\mathsf{T}} \in \mathbb{R}^{2\times 3}. \tag{50}$$

Hence, the measurement matrix becomes

$$\begin{aligned} H_{\text{PARS}} &= (\Pi \hat{R}_{er_j}^\mathsf{T} \quad 0_{2\times 3} \quad 0_{2\times 3} \quad 0_{2\times 3} \quad 0_{2\times 3} \quad 0_{2\times 3m}) \\ &\in \mathbb{R}^{2\times(15+3m)}. \end{aligned} \tag{51}$$

Furthermore, the covariance of $\mathbf{y}_{\text{PARS}}^{r_j}$ can be computed using

$$\mathcal{R}_{\text{PARS}}^{r_j} = \mathbf{M}_{\text{PARS}_j} \mathcal{R}_{\text{PARS}} \mathbf{M}_{\text{PARS}_j}^{\mathsf{T}} \tag{52}$$

where

$$\mathcal{R}_{\text{PARS}} = \text{diag}(\mathbb{E}[\varepsilon_\rho^2], \mathbb{E}[\varepsilon_\psi^2]). \tag{53}$$

Here, $\mathcal{R}_{\text{PARS}}$ given in cylindrical coordinates is converted to $\mathcal{R}_{\text{PARS}}^{r_j}$ in Cartesian coordinates [18, Ch. 1.6]. $\mathbf{M}_{\text{PARS}_j}$ is a Jacobian matrix of $\mathbf{y}_{\text{PARS}}^{r_j}$ with respect to the noise $\boldsymbol{\varepsilon}_{\text{PARS}} = (\varepsilon_\rho, \varepsilon_\psi)$:

$$\mathbf{M}_{\text{PARS}_j} = \frac{\partial \mathbf{y}_{\text{PARS}}^{r_j}}{\partial \boldsymbol{\varepsilon}_{\text{PARS}}} = \begin{pmatrix} m_{11} & m_{12} \\ m_{21} & m_{22} \end{pmatrix} \tag{54}$$

with

$$m_{11} = \frac{\cos(\psi_{y_j})\rho_{y_j}}{\bar{\rho}_{y_j}} \quad m_{12} = -\sin(\psi_{y_j})\bar{\rho}_{y_j}$$

$$m_{21} = \frac{\sin(\psi_{y_j})\rho_{m_j}}{\bar{\rho}_{y_j}} \quad m_{22} = \cos(\psi_{y_j})\bar{\rho}_{y_j}.$$

In a practical implementation $\hat{\mathbf{p}}_{eb}^e$ is used instead of $\mathbf{p}_{eb}^e$ in Eq. 47 such that

$$\bar{\rho}_{y_j} \approx \rho_{y_j} \frac{\hat{\mathbf{p}}_{eb}^e \cdot \mathbf{p}_{er_j}^e}{\|\hat{\mathbf{p}}_{eb}^e\|_2 \|\mathbf{p}_{er_j}^e\|_2}, \tag{55}$$

which is valid for small $\|\delta\mathbf{p}_{eb}^e\|_2$.

4.3.2 Barometer

Atmospheric pressure measurements from barometer can be converted to the altitude of UAV from the sea level using [16, Eq. (6.19)]

$$y_{\text{baro}} = \frac{T_0}{K_t}\left[\left(\frac{P_b}{P_0}\right)^{-\left(\frac{R_t K_t}{g_0}\right)} - 1\right] \tag{56}$$

where

P_0: sea level surface pressure
T_0: sea level surface temperature
P_b: ambient air pressure measured by barometer
R_t: gas constant
K_t: atmospheric temperature gradient
g_0: average surface acceleration due to gravity.

The barometric altitude measurement y_{baro} can then be related to the position using

$$y_{\text{baro}} = \|\hat{\mathbf{p}}_{eb}^e + \delta\mathbf{p}_{eb}^e - \mathbf{p}_{es}^e\|_2 + \varepsilon_{\text{baro}} + b_{\text{baro}} \tag{57}$$

where $\mathbf{p}_{es}^e$ denotes the ECEF position of the geoid (approximate Earth's surface) below the UAV position, b_{baro} represent the barometer's altitude bias [3] and $\varepsilon_{\text{baro}}$ is the measurement noise. The rational behind Eq. 57 is that the altitude is distance between the geoide/surface to the UAV. The Jacobian matrix of y_{baro} with respect to $\delta\mathbf{p}_{eb}^e$ can be computed by differentiating Eq. 57

$$\left.\frac{\partial y_{\text{baro}}}{\partial\delta\mathbf{p}_{eb}^e}\right|_{\delta\mathbf{p}_{eb}^e=\mathbf{0}_{3\times1}} = \underbrace{\frac{(\hat{\mathbf{p}}_{eb}^e - \mathbf{p}_{es}^e)^{\mathsf{T}}}{\|\hat{\mathbf{p}}_{eb}^e - \mathbf{p}_{es}^e\|}}_{\mathbf{H}_{\text{alt}}} \in \mathbb{R}^{1\times3} \tag{58}$$

such that the measurement matrix becomes

$$\mathbf{H}_{\text{baro}} = (\mathbf{H}_{\text{alt}}\ \mathbf{0}_{1\times3}\ \mathbf{0}_{1\times3}\ \mathbf{0}_{1\times3}\ \mathbf{0}_{1\times3}\ \mathbf{0}_{1\times3m}) \in \mathbb{R}^{1\times(15+3m)}, \tag{59}$$

and the measurement covariance matrix is simply

$$\mathcal{R}_{\text{baro}} = \mathbb{E}[\varepsilon_{\text{baro}}^2]. \tag{60}$$

The vector $\mathbf{p}_{es}^e$ can be calculated in two stages. First, the geodetic height, h_s can be calculated from the estimated latitude, $\hat{\mu}$, and longitude, $\hat{\lambda}$, of the UAV using e.g. Earth Gravity Model (EGM) 96 or 2008. In the second stage $\mathbf{p}_{es}^e$ is calculated using

$$\mathbf{p}_{es}^e = \begin{pmatrix} (R_N + h_s)\cos(\hat{\mu})\cos(\hat{\lambda}) \\ (R_N + h_s)\cos(\hat{\mu})\sin(\hat{\lambda}) \\ (R_N(1 - e^2) + h_s)\sin(\hat{\mu}) \end{pmatrix} \tag{61}$$

where $R_N = a(1 - e^2\sin^2(\hat{\mu}))^{-1/2}$ is the WGS84 ellipsoid's semi major axis and e is the ellipsoid's eccentricity.

4.4 Multiplicative Extended Kalman Filter

Using the motion model and the measurement models presented in Sections 4.1, 4.2 and 4.3, MEKF is propagated. The procedure is similar for both mode 1 and mode 2. The MEKF at time k is computed in the following order:

1. Update nominal state using a discrete-time implementation of Eq. 25

---

[3] The barometer bias was compensated from pre-flight, but can also be estimated real-time when GNSS is available [16, Ch. 16.2.2].

2. Propagate the covariance $\mathcal{P}[k]$ of $\delta\boldsymbol{x}[k] \sim \mathcal{N}(0, \mathcal{P}[k])$

$$\hat{\mathcal{P}}[k] = \boldsymbol{F}_d[k-1]\mathcal{P}[k-1]\boldsymbol{F}_d[k-1]^\mathsf{T} + \mathcal{Q}[k-1] \quad (62)$$

where $\boldsymbol{F}_d[k]$ and $\mathcal{Q}[k]$ can be calculated or approximated using van Loan based on $\boldsymbol{F}(t)$, $\boldsymbol{G}(t)$ and $\mathcal{Q}(t)$ matrices

3. If any measurements are available,

   (a) Compute the Kalman gain

   $$\boldsymbol{K}[k] = \hat{\mathcal{P}}[k]\boldsymbol{H}_\star^\mathsf{T}[k](\boldsymbol{H}_\star[k]\hat{\mathcal{P}}[k]\boldsymbol{H}_\star^\mathsf{T}[k] + \mathcal{R}_\star[k])^{-1}$$
   $$(63)$$

   (b) Calculate the estimated error

   $$\delta\boldsymbol{x}[k] = \boldsymbol{K}[k](\boldsymbol{y}_\star[k] - \hat{\boldsymbol{y}}_\star[k]) \quad (64)$$

   (c) Correct the nominal state using Eq. 23

   (d) Update the estimation error covariance

   $$\mathcal{P}[k] = (\boldsymbol{I} - \boldsymbol{K}[k]\boldsymbol{H}_\star[k])\hat{\mathcal{P}}[k](\boldsymbol{I} - \boldsymbol{K}[k]\boldsymbol{H}_\star[k])^\mathsf{T}$$
   $$+ \boldsymbol{K}[k]\boldsymbol{R}_\star[k]\boldsymbol{K}[k]^\mathsf{T} \quad (65)$$

   (e) Set the error state to zero

   $$\delta\boldsymbol{x} = \boldsymbol{0}_{(15+3m)\times 1} \quad (66)$$

Here, prediction step corresponds to 1) and 2), and correction step corresponds to 3).

4.5 Outlier Rejection

As mentioned in Section 1, the PARS measurements are sometimes very noisy due to reflections from water surface. Outlier rejection was implemented to prevent bad PARS measurements from degrading the estimation. If the test statistic

$$T(\boldsymbol{y}_\star) = (\boldsymbol{y}_\star - \hat{\boldsymbol{y}}_\star)^\mathsf{T}(\boldsymbol{H}_\star \hat{P}\boldsymbol{H}_\star^\mathsf{T} + \mathcal{R}_\star)^{-1}(\boldsymbol{y}_\star - \hat{\boldsymbol{y}}_\star) \sim \chi_1^2 \quad (67)$$

is above some limit χ_α^2, the measurement is discarded as outlier [19, Section 7.6.1].

5 Practical Aspects

A field test was conducted on October 8th 2020 in good weather conditions at the north of Agdenes outside Trondheim, Norway. We performed multiple flights with a Skywalker X8 UAV and *two* ground antennas for PARS. Before conducting the flights, we measured the the position and the orientation of the PARS ground antennas by GNSS and a compass. During the flights, we recorded multiple sensor measurements and autopilot solutions from a Pixhawk autopilot in addition to independent IMU, RTK-GNSS
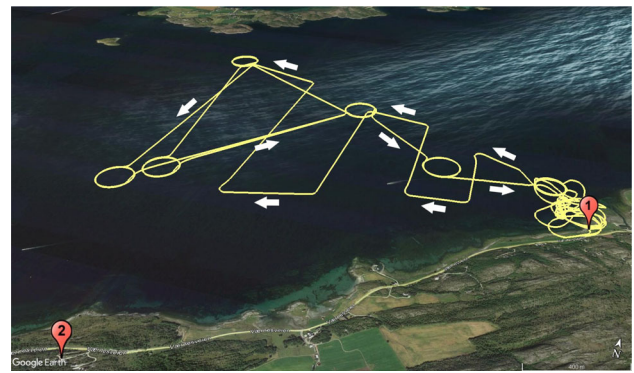

Fig. 5 Flight path of the UAV based on RTK GNSS with ground antenna positions indicated

and PARS measurements with corresponding timestamps. Figure 5 indicates the flight path with directional arrows and ground antenna positions. Figure 6 gives an overview of the hardware system used in this field test.

5.1 Payload

The UAV avionics included a Pixhawk autopilot running ArduPlane flight control software with a 3DR GPS module, a Honeywell HMC5883L 3-axis digital compass IC, MS561101BA03 barometric pressure sensor, and an internal IMU/INS. In addition to the Pixhawk autopilot, the payload was equipped with a tactical grade IMU, the Sen-
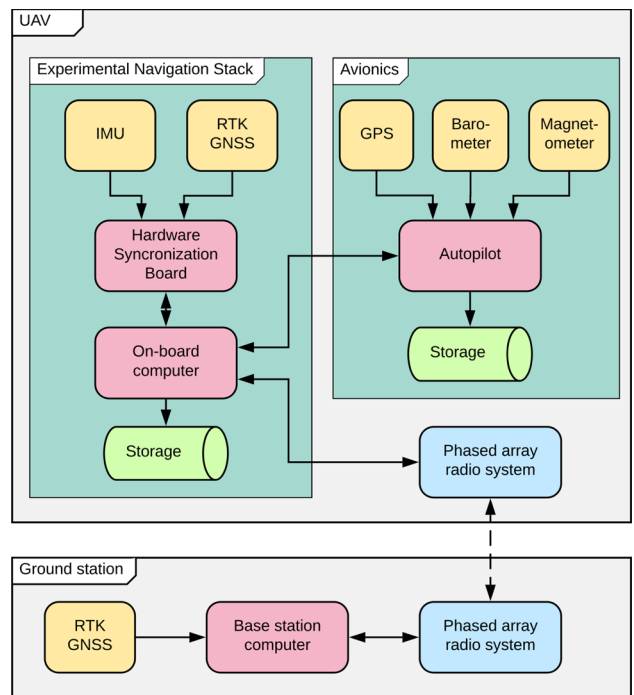

Fig. 6 System overview

sonor STIM 300, and a Ublox F9PZED GNSS receiver to enable accurate RTK GNSS measurements. A SenTiBoard [20] was used to synchronize the timestamps of the IMU and GNSS measurements. This synchronization can facilitate the integration of measurements in an Odroid XU4 onboard computer. Radionor Communications PARS CRE2 144LW sent telemetry data to the ground station and received commands and PARS measurements. A 433 MHz 3DR radio was used as a redundant telemetry link to meet redundancy requirements for BLOS flights. References [5, 9] provide more details on the payload.

5.2 Ground Station

A ground station was set up to compute RTK GNSS data, PARS positioning data, and to remotely pilot the UAV. The ground station consisted of a laptop computer, a uBlox F9P-ZED GNSS receiver, and two Radionor Communications CRE2-189 PARS. The CRE2-189 is a ground radio system covering a 90° frustum both in elevation and in azimuth with an root mean square error of 0.1° in each axis. The second antenna was set approximately perpendicular to the first antenna with a 2.6 km separation between the two antennas. The PARS was set to a 2 Mbit/s mode with a maximal distance of up to 60 km.

5.3 Initial Calibration

As shown in Section 3.2, PARS delivers a position measurement in the local radio frame $\{r\}$. Therefore, it is important to calibrate the mounting angles of ground antennas to estimate the UAV's position accurately. As the algorithm shown in Section 4.2.2 requires reasonably accurate initial estimates, we measured the mounting angles of antennas with a compass. However, the compass only gave a roughly known angle because the compass reading changes when close to a metal antenna. While the full orientation consists of the roll, pitch, and yaw angles, we measured only the yaw angle as the roll and pitch angles are close enough to zero and were considered reasonable for the initial estimates. The positions of the PARS ground antennas were identified with a GNSS receiver.

6 Results and Discussion

Using the tactical grade IMU, the RTK-GNSS, the PARS and the Pixhawk barometer measurements obtained from the field test described in Section 5, offline calculations were carried out to validate the navigation system presented in Section 4 (MEKF-based aided-INS using barometer and PARS measurements, which performs in-flight calibration when RTK-GNSS is available). The solutions from the navigation system were verified by the attitude and the velocity

solutions from the Pixhawk autopilot and the position measurements from the RTK-GNSS. In the offline calculations, rough estimates of the first and the second antenna orientation measured by a compass were used as an initial state:

$$\mathbf{\Theta}_{\mathrm{PARS}_1} = (\phi_{r_1}, \theta_{r_1}, \psi_{r_1}) = (0°, 0°, -65.5°) \tag{68}$$

$$\mathbf{\Theta}_{\mathrm{PARS}_2} = (\phi_{r_2}, \theta_{r_2}, \psi_{r_2}) = (0°, 0°, 26.7°). \tag{69}$$

Numerical values for the covariance matrices $\mathbf{Q}$ and $\mathbf{R}_\star$, and the parameters for Eq. 56 can be found in the Appendix C. The $\chi_\alpha^2 = 7.815$ was chosen as the outlier rejection threshold.

The GNSS measurements were made available between 1000s-1200s at the midpoint of the flight when the UAV was flying the furthest part of the path. This means that before 1000s, the INS used PARS measurements with the rough estimates of the antenna orientations from Eqs. 68 and 69 as an aid (Mode 2). Once the GNSS measurements became available, the INS switched to use GNSS measurements and calibration of the antenna mounting angles started (Mode 1). After GNSS outage at 1200s, the calibration stopped, and the INS switched back to solely use PARS measurements with calibrated mounting angles (Mode 2 again).

Figure 7 shows the antenna orientation estimates in Euler angles. The calibration algorithm successfully estimated the antenna mounting angles fairly quickly (by 1050s) using the position estimates from the GNSS-aided INS, even though the initial estimates contained approximately 10° of errors.

Figure 8 presents the position, velocity and attitude estimates from the aided-INS. The solutions from aided-INS are denoted as *Calibration MEKF (ECEF)*, and shown with orange lines.

In Figs. 8a and b, the attitude and the velocity from the aided-INS are compared to the heading reference (AHRS) and the velocity from the autopilot (Pixhawk). The autopilot solutions are denoted as *pixhawk: ahrs* and *pixhawk: vel3d* respectively, and shown with blue lines in the figures. Considering that the Pixhawk uses relatively low-cost sensors, its solution is not sufficiently accurate to be regarded as a ground truth. However, as it provides attitude and velocity solutions which are independent from the aided-INS, and is a well-established navigation solution for closed-loop flight, it is considered as an appropriate reference. The attitude and velocity estimates did not change significantly between before and after the calibration.

Figures 8c and d evaluates the position estimate from the aided-INS by comparing it to RTK-GNSS solution, where Fig. 8e shows the transition part of Fig. 8d. The RTK-GNSS solution was denoted as *rtk: pos3d*, and shown with blue lines in the figures. As RTK-GNSS solution has centimeter-level accuracy, it is sufficient to be considered as a ground truth. The red star in Figs. 8d and e, and the blue star in Fig. 8d indicate the start and the end points of the calibration, respectively, where the arrows indicate the direction of the
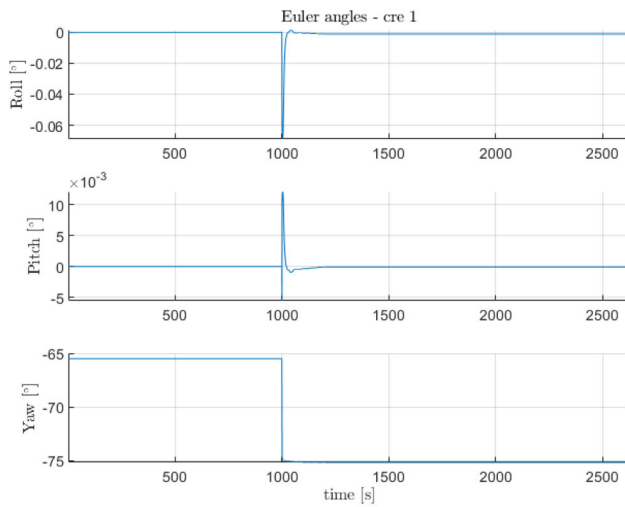
(a) The first antenna with $\psi_{r_1} = -65.5°$
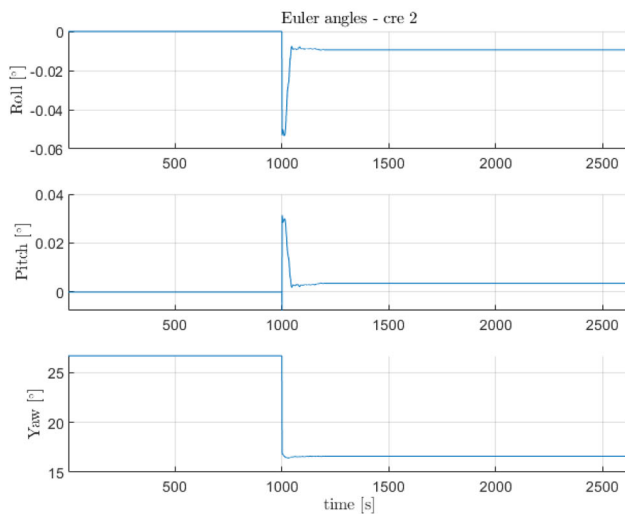
(b) The second antenna with $\psi_{r_2} = 26.7°$

Fig. 7 Euler angles of antenna orientations

UAV. A significant change between before and after the calibration can be seen in the position estimate plot. The orange line (aided-INS) is shifted from the blue-line (RTK-GNSS) when using the rough estimates of antenna orientation (before the calibration), while the orange line fits well with the blue line when using the accurate orientation estimates (after the calibration).

Tables 1, 2, and 3 show mean-error (ME), absolute mean-error (AME), standard deviation (STD) and root mean square error (RMSE) statistics of the aided-INS estimates for before (0s-1000s), during (1000s-1200s) and after (1200s-2625s) the calibration, denoted as *PARS + Baro/INS: Pre calib.*, *PARS + GNSS/INS: Mid. calib.* and *PARS + Baro/INS: After calib.* respectively, using the autopilot solution as a reference. Essentially, the values before and after the calibration

are from PARS-aided (and barometer-aided) INS, while the values during calibration are from GNSS-aided (and PARS-aided) INS. Slight but some improvements can be seen in the attitude and the velocity statistics before and after the calibration. Error in the yaw angle is larger than the errors in the roll and pitch angles, and this corresponds to the larger error in the north and the east direction compared to the error in the Down direction of the velocity and the position statistics. While the attitude and velocity statistics did not change much before and after the calibration, the position statistics improved significantly. The position statistics during calibration is better than after calibration because GNSS was aiding the INS. As barometer measurements aided the altitude, the
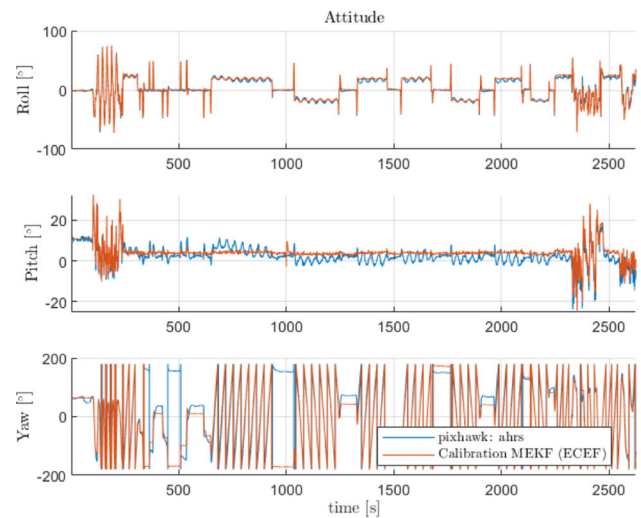
(a) Attitude solution compared to Pixhawk autopilot reference
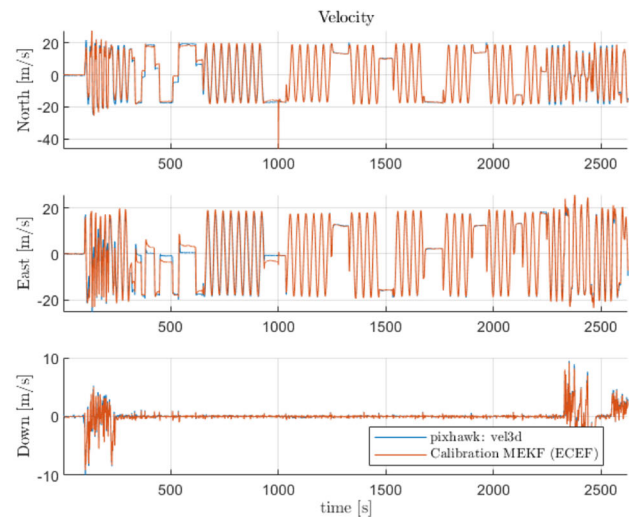
(b) Velocity solution compared to Pixhawk autopilot reference

Fig. 8 Attitude, Velocity and Position solutions from the aided-INS (orange) compared to Pixhawk autopilot or RTK-GNSS references (blue)

**Table 1** Attitude error statistics before (top), during (middle) and after (bottom) calibration

		Roll [°]	Pitch [°]	Yaw [°]	Norm [°]
PARS± Baro/INS: Pre calib.	ME:	-0.62	0.88	-11.42	11.47
	AME:	1.98	1.65	17.80	17.99
	STD:	2.73	1.94	18.00	18.31
	RMSE:	2.80	2.13	21.31	21.60
PARS± GNSS/INS: Mid. calib.	ME:	-2.95	0.24	-14.13	14.44
	AME:	3.08	1.14	14.25	14.62
	STD:	1.67	1.38	12.46	12.64
	RMSE:	3.39	1.40	18.84	19.19
PARS± Baro/INS: After calib.	ME:	-2.68	0.97	5.26	5.98
	AME:	2.84	2.17	13.44	13.90
	STD:	2.08	2.74	15.81	16.18
	RMSE:	3.39	2.91	16.66	17.25

Table 2 Velocity error statistics before (top), during (middle) and after (bottom) calibration

		North [m/s]	East [m/s]	Down [m/s]	Norm [m/s]
PARS± Baro/INS: Pre calib.	ME:	-0.46	-0.12	0.05	0.48
	AME:	1.59	2.00	0.13	2.55
	STD:	1.91	2.33	0.22	3.02
	RMSE:	1.96	2.34	0.22	3.06
PARS± GNSS/INS: Mid. calib.	ME:	0.09	-0.10	-0.02	0.14
	AME:	0.34	0.21	0.07	0.41
	STD:	1.57	0.33	0.09	1.61
	RMSE:	1.57	0.35	0.09	1.61
PARS± Baro/INS: After calib.	ME:	0.00	0.03	0.04	0.05
	AME:	0.41	0.40	0.10	0.58
	STD:	0.65	0.61	0.15	0.90
	RMSE:	0.65	0.61	0.16	0.91

Table 3 Position error statistics before (top) during (middle) and after (bottom) calibration

		North [m]	East [m]	Down [m]	Norm [m]
PARS± Baro/INS: Pre calib.	ME:	-223.19	-101.28	0.58	245.09
	AME:	223.37	112.03	0.82	249.89
	STD:	159.97	114.99	0.94	197.01
	RMSE:	274.59	153.23	1.10	314.46
PARS± GNSS/INS: Mid. calib.	ME:	-0.02	-0.01	0.01	0.03
	AME:	0.14	0.06	0.03	0.16
	STD:	0.45	0.10	0.05	0.47
	RMSE:	0.45	0.10	0.05	0.47
PARS± Baro/INS: After calib.	ME:	-2.98	7.79	-0.47	8.35
	AME:	3.96	7.94	0.67	8.90
	STD:	6.94	10.36	0.74	12.49
	RMSE:	7.55	12.96	0.87	15.03
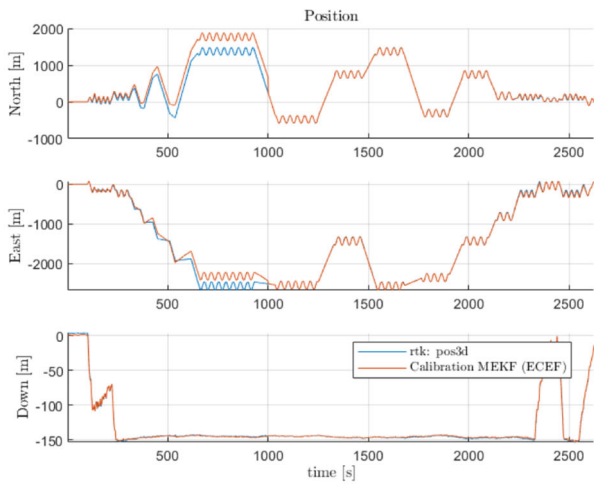
(c) Position solution compared to RTK-GNSS reference in 1D
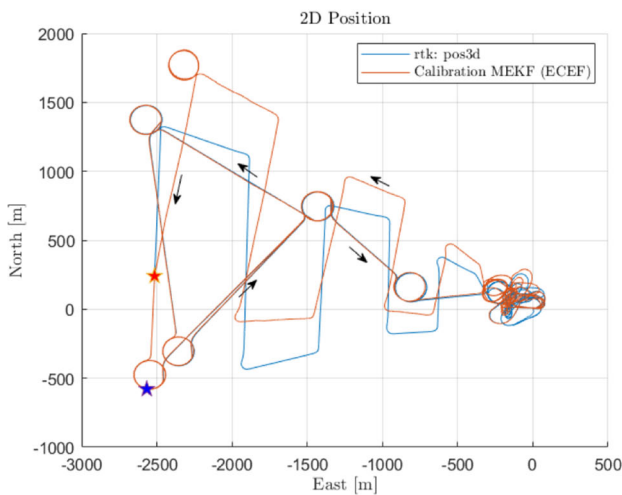
(d) Position solution compared to RTK-GNSS reference in 2D
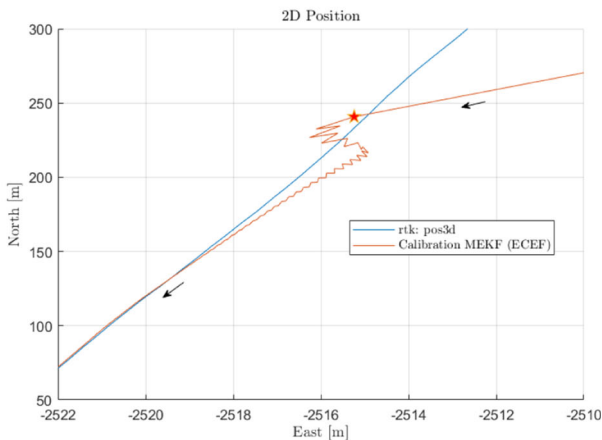
(e) Position during transition compared to RTK-GNSS reference in 2D

Fig. 8 continued

calibration did not affect the position statistics in the Down direction.

In addition to the situation considered above with mounting angles precisely calibrated in the middle of the flight, we also considered a situation that PARS-aided INS uses fixed approximate mounting angles with 0° for pitch and roll and ±2°-3° error in yaw angle

$$\Theta_{PARS_1} = (0°, \ 0°, \ -77°) \tag{70}$$

$$\Theta_{PARS_2} = (0°, \ 0°, \ 19°). \tag{71}$$

throughout the entire flight without calibration, while the calibrated yaw angles for the first and the second ground antennas were -74.927° and 16.627° respectively. The statistics from this additional situation using fixed approximate mounting angles are compared with the statistics with calibrated mounting angles in Table 4. The statistics with fixed mounting was computed over the period 1200s-2625s (equivalent to the duration of after calibration) to directly compare the statistics with precisely calibrated mounting. The attitude, velocity and position statistics are denoted as *Attitude*, *Velocity* and *Position* respectively, with an extra label indicating fixed mounting or calibrated mounting. The calibrated mounting gave slightly better accuracy than the fixed approximate mounting, but the difference was not significant. It seems that the transition from inaccurate initial mounting to precise mounting during the online calibration induced some errors.

Figure 9 compares attitude, velocity and position error plots between the two different situations with the precisely calibrated mounting angles and with the fixed approximate mounting angles. The dotted lines are 3 sigma lines which indicate three times the standard deviation.

In Figs. 9a and b, the attitude error plot exceeds the ± 3 sigma lines through the entire flight. This might be due to the relatively poor precision of Pixhawk reference.

In Fig. 9c, the velocity error plot exceeds the ± 3 sigma lines before calibration, while the error plot drops in the interval after calibration. A spike in the North direction appeared at 1000s when the INS switches from PARS-aided to GNSS-aided.

Similarly, in Fig. 9e, the position error plot improves significantly after calibration. As Figs. 9e and f indicate, errors at the beginning and at the end of the position error plots are relatively large, as the approximation by Eqs. 46–47 is accurate when the range is dominantly larger than the altitude but it becomes worse when the altitude becomes large compared to the range.

Table 4 Error statistics comparison between calibrated mounting (top) and fixed approximate mounting (bottom)

		Roll [°]	Pitch [°]	Yaw [°]	Norm [°]
Attitude: Calibrated	ME:	-2.68	0.97	5.26	5.98
	AME:	2.84	2.17	13.44	13.90
	STD:	2.08	2.74	15.81	16.18
	RMSE:	3.39	2.91	16.66	17.25
Attitude: Fixed	ME:	-2.69	0.95	5.28	6.01
	AME:	2.85	2.17	13.46	13.93
	STD:	2.08	2.75	15.79	16.17
	RMSE:	3.41	2.91	16.65	17.25
		North [m/s]	East [m/s]	Down [m/s]	Norm [m/s]
Velocity: Calibrated	ME:	0.00	0.03	0.04	0.05
	AME:	0.41	0.40	0.10	0.58
	STD:	0.65	0.61	0.15	0.90
	RMSE:	0.65	0.61	0.16	0.91
Velocity: Fixed	ME:	-0.01	0.03	0.04	0.05
	AME:	0.44	0.39	0.10	0.60
	STD:	0.74	0.62	0.15	0.97
	RMSE:	0.74	0.62	0.16	0.98
		North [m]	East [m]	Down [m]	Norm [m]
Position: Calibrated	ME:	-2.98	7.79	-0.47	8.35
	AME:	3.96	7.94	0.67	8.90
	STD:	6.94	10.36	0.74	12.49
	RMSE:	7.55	12.96	0.87	15.03
Position: Fixed	ME:	1.36	8.20	-0.45	8.32
	AME:	4.67	8.67	0.65	9.86
	STD:	6.72	10.74	0.73	12.69
	RMSE:	6.85	13.51	0.85	15.18

7 Conclusion

In this paper, the previously presented calibration algorithm, which estimates the ground antenna orientation for the phased array radio system (PARS), was integrated with the inertial navigation system (INS) aided by multiple sensor measurements. The extended aided-INS switched between two modes to perform the calibration in the middle of a flight whenever GNSS is available. In the first mode, the calibration was performed using the position estimate from GNSS-aided INS as reference. In the second mode, the PARS and the barometer aided the horizontal and the vertical position, respectively. As the vertical measurement of PARS was noisy due to multipath noise, barometer measurement was used as a replacement. To take the Earth's curvature into

consideration, the PARS and the barometer measurements were treated independently and the navigation equations were propagated in the Earth Fixed Earth Centred (ECEF) frame. The independent treatment of PARS and barometer measurements, and the propagation in ECEF frame were also beneficial to provide a common reference point and reference frame among multiple PARS ground antennas. The proposed algorithm was validated by performing offline calculations
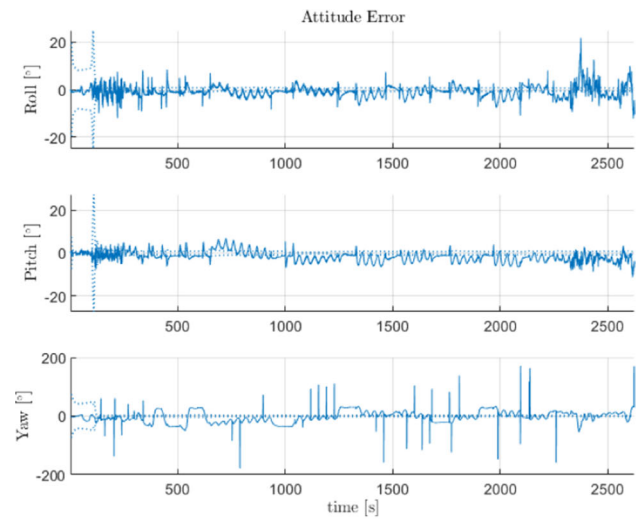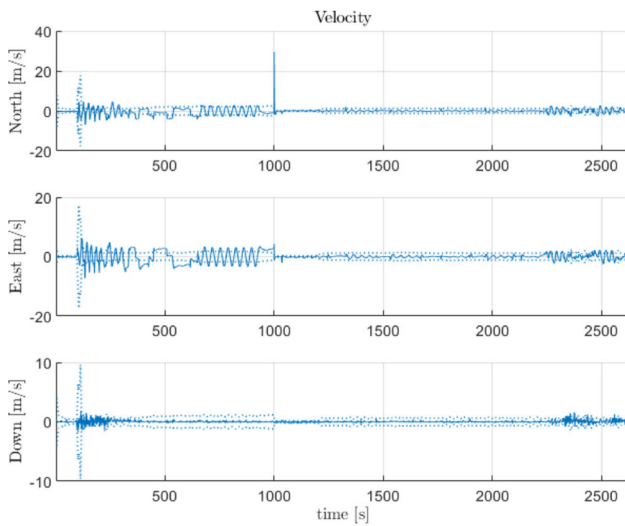

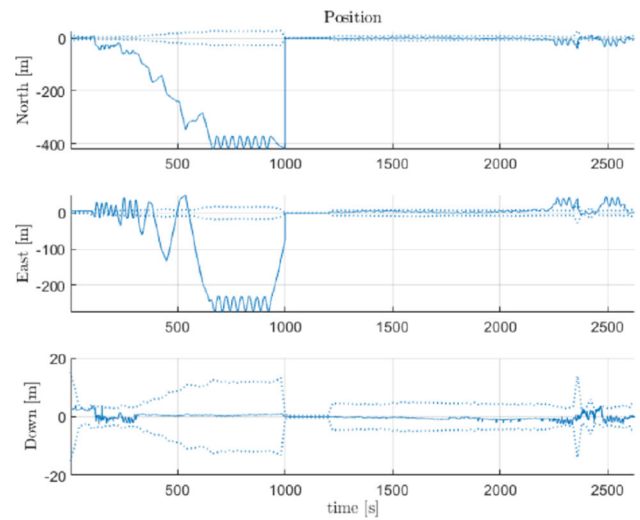(a) Attitude error with calibrated mounting
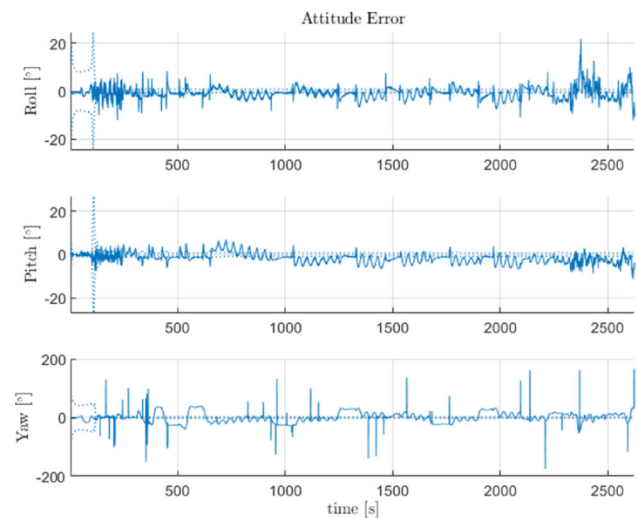
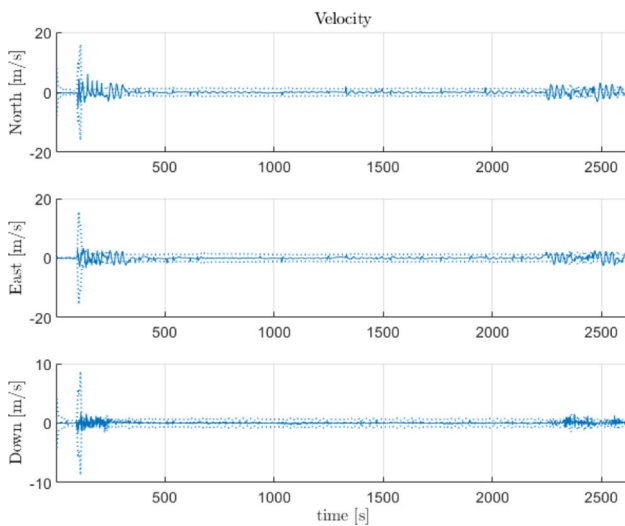(b) Attitude error with fixed approximate mounting

Fig. 9 Error plots w.r.t the autopilot (attitude, velocity) and RTK-GNSS (position) reference. The dotted lines are 3 sigma lines. Calibrated mounting: 0s-1000s (mode 2), 1000s-1200s (mode 1), 1200s-2625s (mode 2) with initial angles indicated in Eqs. 68 and 69, Fixed approximate mounting: mode 2 only with initial angles indicated in Eq. 70 and (71)
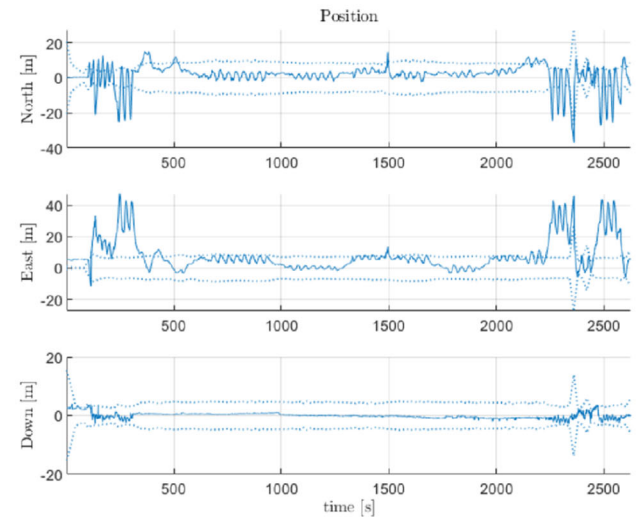
(c) Velocity error with calibrated mounting

(e) Position error with calibrated mounting

(d) Velocity error with fixed approximate mounting

(f) Position error with fixed approximate mounting

Fig. 9 continued

Fig. 9 continued

using the field test data including measurements from IMU, GNSS, Pixhawk autopilot (with barometer) and two PARS ground antennas with making GNSS available in the middle of the flight for 200s. The results were verified by comparing the navigation solutions with GNSS measurements and Pixhawk autopilot solutions. The proposed algorithm successfully estimated the mounting angles of two PARS ground antennas in the middle of flight in 50s and the position estimate significantly improved after the calibration. As a future work, implementation of the proposed method in the onboard embedded system to perform the real-time calculation in the field is in the interest.

Appendix A Jacobian Matrices

The Jacobian matrices in discrete version of the error-state system Eq. 27 are given as

$$
F = \begin{pmatrix}
\mathbf{0}_{3\times3} & \mathbf{I}_3 & \mathbf{0}_{3\times3} & \mathbf{0}_{3\times3} & \mathbf{0}_{3\times3} & \mathbf{0}_{3\times3m} \\
\mathbf{0}_{3\times3} & -2S(\boldsymbol{\omega}_{ie}^e) & \mathbf{V}_a & \mathbf{V}_{acc} & \mathbf{0}_{3\times3} & \mathbf{0}_{3\times3m} \\
\mathbf{0}_{3\times3} & \mathbf{0}_{3\times3} & \mathbf{A}_a & \mathbf{0}_{3\times3} & \mathbf{A}_{ars} & \mathbf{0}_{3\times3m} \\
\mathbf{0}_{3\times3} & \mathbf{0}_{3\times3} & \mathbf{0}_{3\times3} & -\mathbf{T}_{acc}^{-1} & \mathbf{0}_{3\times3} & \mathbf{0}_{3\times3m} \\
\mathbf{0}_{3\times3} & \mathbf{0}_{3\times3} & \mathbf{0}_{3\times3} & \mathbf{0}_{3\times3} & -\mathbf{T}_{ars}^{-1} & \mathbf{0}_{3\times3m} \\
\mathbf{0}_{3m\times3} & \mathbf{0}_{3m\times3} & \mathbf{0}_{3m\times3} & \mathbf{0}_{3m\times3} & \mathbf{0}_{3m\times3} & \mathbf{0}_{3m\times3m}
\end{pmatrix}
$$

$$\in \mathbb{R}^{(15+3m)\times(15+3m)} \quad \text{(A1)}$$

$$
G = \begin{pmatrix}
\mathbf{0}_{3\times3} & \mathbf{0}_{3\times3} & \mathbf{0}_{3\times3} & \mathbf{0}_{3\times3} & \mathbf{0}_{3\times3m} \\
-R_b^e(q_b^e) & \mathbf{0}_{3\times3} & \mathbf{0}_{3\times3} & \mathbf{0}_{3\times3} & \mathbf{0}_{3\times3m} \\
\mathbf{0}_{3\times3} & -I_3 & \mathbf{0}_{3\times3} & \mathbf{0}_{3\times3} & \mathbf{0}_{3\times3m} \\
\mathbf{0}_{3\times3} & \mathbf{0}_{3\times3} & I_3 & \mathbf{0}_3 & \mathbf{0}_{3\times3m} \\
\mathbf{0}_{3\times3} & \mathbf{0}_{3\times3} & \mathbf{0}_{3\times3} & I_3 & \mathbf{0}_{3\times3m} \\
\mathbf{0}_{3m\times3} & \mathbf{0}_{3m\times3} & \mathbf{0}_{3m\times3} & \mathbf{0}_{3m\times3} & \mathbf{0}_{3m\times3m}
\end{pmatrix}
$$
$$
\in \mathbb{R}^{(15+3m)\times(12+3m)} \quad \text{(A2)}
$$

where

$$
V_a = -\hat{R}_{eb}(q_b^e)S(f_{\text{IMU}}^b - \hat{b}_{acc}^b)
$$
$$
V_{\text{acc}} = -\hat{R}_{eb}(q_b^e)
$$
$$
A_a = -S\left(\omega_{\text{IMU}}^b - \hat{b}_{ars}^b - \hat{R}_{eb}^\top \omega_{ie}^e\right)
$$
$$
A_{\text{ars}} = -I_3.
$$

The process noise effecting the velocity, orientation and bias estimates error $w = (\varepsilon_{acc}^\top, \varepsilon_{ars}^\top, \varepsilon_{b_{acc}}^\top, \varepsilon_{b_{ars}}^\top, \varepsilon_{\delta a_1}^\top, \ldots, \varepsilon_{\delta a_m}^\top)^\top$ are modeled by white Gaussian processes. The total spectral density is given as

$$
\mathcal{Q} = \begin{pmatrix}
V_\epsilon & \mathbf{0}_{3\times3} & \mathbf{0}_{3\times3} & \mathbf{0}_{3\times3} & \mathbf{0}_{3\times3m} \\
\mathbf{0}_{3\times3} & \Theta_\epsilon & \mathbf{0}_{3\times3} & \mathbf{0}_{3\times3} & \mathbf{0}_{3\times3m} \\
\mathbf{0}_{3\times3} & \mathbf{0}_{3\times3} & A_\epsilon & \mathbf{0}_{3\times3} & \mathbf{0}_{3\times3m} \\
\mathbf{0}_{3\times3} & \mathbf{0}_{3\times3} & \mathbf{0}_{3\times3} & \Omega_\epsilon & \mathbf{0}_{3\times3m} \\
\mathbf{0}_{3m\times3} & \mathbf{0}_{3m\times3} & \mathbf{0}_{3m\times3} & \mathbf{0}_{3m\times3} & C_\epsilon
\end{pmatrix}
$$
$$
\in \mathbb{R}^{(12+3m)\times(12+3m)} \quad \text{(A3)}
$$

where

$$V_\epsilon = \sigma_{\text{acc}}^2 I_3 \qquad [\text{m}^2\text{s}^{-3}] \qquad \text{(A4)}$$
$$\Theta_\epsilon = \sigma_{\text{ars}}^2 I_3 \qquad [\text{rad}^2\text{s}^{-1}] \qquad \text{(A5)}$$
$$A_\epsilon = \sigma_{b_{acc}}^2 I_3 \qquad [\text{m}^2\text{s}^{-5}] \qquad \text{(A6)}$$
$$\Omega_\epsilon = \sigma_{b_{ars}}^2 I_3 \qquad [\text{rad}^2\text{s}^{-3}] \qquad \text{(A7)}$$
$$C_\epsilon = \sigma_{\text{calib}}^2 I_m \qquad [\text{rad}^2\text{s}^{-1}], \qquad \text{(A8)}$$

and the receive spectral densities are calculated

$$\sigma_\star^2 = \mathbb{E}[\varepsilon_\star(t)\varepsilon_\star^\top(\tau)]. \qquad \text{(A9)}$$

Appendix B Calibration Algorithm

The measurement model is formulated based on the following relationship between the UAV position (p_{eb}^e), the ground station position ($p_{er_j}^e$) and UAV PARS position relative to the ground radio ($p_{r_jb}^{r_j}$):

$$p_{eb}^e = p_{er_j}^e + R_{en_j} R_{n_j r_j} p_{r_jb}^{r_j}. \qquad \text{(B10)}$$

Firstly, moving $p_{er_j}^e$ from RHS to LHS yields

$$p_{eb}^e - p_{er_j}^e = R_{en_j} R_{n_j r_j} p_{r_jb}^{r_j}. \qquad \text{(B11)}$$

By multiplying both sides by $R_{en_j}^\top$ and using $R_{n_j r_j} = \hat{R}_{n_j r_j}(I_3 + S(\delta a))$,

$$R_{en_j}^\top(p_{eb}^e - p_{er_j}^e) = R_{en_j}^\top R_{en_j} R_{n_j r_j} p_{r_jb}^{r_j} \qquad \text{(B12)}$$
$$= \hat{R}_{n_j r_j}(I_3 + S(\delta a)) p_{r_jb}^{r_j} \qquad \text{(B13)}$$
$$= \hat{R}_{n_j r_j} p_{r_jb}^{r_j} + \hat{R}_{n_j r_j} S(\delta a) p_{r_jb}^{r_j}. \qquad \text{(B14)}$$

Swapping cross product between $p_{r_jb}^{r_j}$ and δa yields

$$R_{en_j}^\top\left(p_{eb}^e - p_{er_j}^e\right) = \hat{R}_{n_j r_j} p_{r_jb}^{r_j} - \hat{R}_{n_j r_j} S\left(p_{r_jb}^{r_j}\right) \delta a_{r_j}^{n_j}, \qquad \text{(B15)}$$

and by moving the δa from the left to right side,

$$\hat{R}_{n_j r_j} p_{r_jb}^{r_j} = R_{en_j}^\top\left(p_{eb}^e - p_{er_j}^e\right) + \hat{R}_{n_j r_j} S\left(p_{r_jb}^{r_j}\right) \delta a_{r_j}^{n_j}. \qquad \text{(B16)}$$

Finally, by substituting $p_{eb}^e = \hat{p}_{eb}^e + \delta p_{eb}^e$, the final equation is formulated:

$$\underbrace{\hat{R}_{n_j r_j} p_{r_jb}^{r_j}}_{y_{\text{pars}_j}} = \underbrace{R_{en_j}^\top\left(\hat{p}_{eb}^e - p_{er_j}^e\right)}_{\hat{y}_{\text{pars}_j}} + \underbrace{R_{en_j}^\top \delta p}_{H_{\text{pos}_j}}$$
$$+ \underbrace{\hat{R}_{n_j r_j} S\left(p_{r_jb}^{r_j}\right) \delta a_{r_j}^{n_j}}_{H_{\text{calib}_j}} \qquad \text{(B17)}$$

Appendix C Numerical Values

Numerical values for the matrices $\mathcal{Q}$ and $R_\star$ were set as

$$\sigma_{\text{acc}} = 47.85\,\text{m s}^{-1.5}$$
$$\sigma_{\text{ars}} = 5.35 \times 10^{-7}\,\text{rad s}^{0.4}$$
$$\sigma_{b_{acc}} = 4.91 \times 10^{-3}\,\text{m s}{-2.5}$$
$$\sigma_{b_{ars}} = 1.74 \times 10^{-7}\,\text{rad s}^{-1.5}$$
$$\sigma_{\text{calib}} = 0\,\text{rad s}^{0.5},$$

where σ_{calib} is zero because the antennas are stationary, and

$$\sigma_\rho = 15\,\text{m} \qquad\qquad \sigma_{\text{gnss},x} = 0.2\,\text{m}$$
$$\sigma_\psi = 2° \qquad\qquad \sigma_{\text{gnss},y} = 0.2\,\text{m}$$
$$\sigma_{\text{baro}} = 5\,\text{m} \qquad\qquad \sigma_{\text{gnss},z} = 0.4\,\text{m}$$
$$\sigma_{\text{alt}} = 5\,\text{m}.$$

The parameters for Eq. 56 were chosen to be

$$P_0 = 10040 \, Pa$$
$$T_0 = 280.15 \, K$$
$$R_t = 287.7 \, J kg^{-1} K^{-1}$$
$$K_t = 6.5 \times 10^{-3} \, K m^{-1}$$
$$g_0 = 9.807 \, ms^{-2}.$$

The numerical values for R_t, K_t and g_0 were chosen from [16, Ch. 6.2.1], and P_0 and T_0 are based on the local temperature and atmospheric pressure on the field test day.

Author Contributions All authors of the paper constitute an author according to the Journal's and Publisher's requirements. Mika Okuhara drafted the manuscript and performed the analysis of data. Torleiv H. Bryne made the software architecture. Kristoffer Gryte carried out field tests and collected data. All authors read the the manuscript, made contributions to the concept design and the final manuscript.

Availability of data and materials Not applicable

Code Availability Not applicable

Declarations

Ethics approval Not applicable

Consent to participate Not applicable

Consent for publication The authors have consent for publication.

Conflict of interest The authors have no conflicts of interest to declare that are relevant to the content of this article.

References

1. Pinker, A., Smith, C.: Vulnerability of the GPS signal to jamming. GPS Solutions **3**(2), 19–27 (1999)

2. Kerns, A.J., Shepard, D.P., Bhatti, J.A., Humphreys, T.E.: Unmanned aircraft capture and control via GPS spoofing. J. Field Robot. **31**(4), 617–636 (2014)

3. Albrektsen, S.M., Soegrov, A., Johansen, T.A.: Navigation of uav using phased array radio. In: Workshop on research, education and development of unmanned aerial systems (RED UAS), pp. 138–143 (2017)

4. Albrektsen, S.M., Bryne, T.H., Johansen, T.A.: Phased array radio system aided inertial navigation for unmanned aerial vehicles. In: Proceedings of the IEEE aerospace conference, Big Sky, Montana, pp. 1–11 (2018)

5. Albrektsen, S.M., Bryne, T.H., Johansen, T.A.: Robust and secure uav navigation using gnss, phased-array radiosystem and inertial sensor fusion. In: 2nd IEEE Conference on control technology and applications, copenhagen, Denmark, pp. 1338–1345 (2018)

6. Gryte, K., Bryne, T.H., Albrektsen, S.M., Johansen, T.A.: Field test results of gnss-denied inertial navigation aided by phased-array radio systems for uavs. In: 2019 International conference on unmanned aircraft systems (ICUAS), pp. 1398–1406 (2019)

7. Solà, J.: Quaternion kinematics for the error-state Kalman filter (2017)

8. Markley, F.L.: Attitude error representation for kalman filtering. J. Guid. Control Dyn. **26**(2), 311–317 (2003)

9. Gryte, K., Bryne, T.H., Johansen, T.A.: Unmanned aircraft flight control aided by phased-array radio navigation. J.Field Robot. 1–20 (2020)

10. Okuhara, M., Bryne, T.H., Gryte, K., Johansen, T.A.: Phased array radio navigation system on uavs: Gnss-based calibration in the field. In: 2021 International conference on unmanned aircraft systems (ICUAS), pp. 210–218 (2021). https://doi.org/10.1109/ICUAS51884.2021.9476807

11. Farrell, J.A.: Aided Navigation: GPS with High Rate Sensors, 1st edn. McGraw-Hill Inc, Maidenhead (2008)

12. Titterton, D.H., Weston, J.L.: Strapdown Inertial Navigation Technology, 2nd edn. Inst. Electr. Eng. Am. Inst. Aeronaut. Astronaut, Stevenage (2004)

13. Krim, H., Viberg, M.: Two decades of array signal processing research: the parametric approach. IEEE Sign. Process. Mag. **13**(4), 67–94 (1996)

14. Roy, R., Kailath, T.: ESPRIT-estimation of signal parameters via rotational invariance techniques. IEEE Trans. Acoust. Speech Signal Process. **37**(7), 984–995 (1989)

15. Schmidt, R.: Multiple emitter location and signal parameter estimation. IEEE Trans Antennas Propag. **34**(3), 276–280 (1986)

16. Groves, P.D.: Principles of GNSS, Inertial, and Multisensor Integrated Navigation Systems, 2nd edn. Artech House, Boston (2013)

17. Roumeliotis, S.I., Sukhatme, G.S., Bekey, G.A.: Circumventing dynamic modeling: Evaluation of the error-state kalman filter applied to mobile robot localization. In: IEEE International conference on robotics and automation, Detroit, Michigan, pp. 1656–1663 (1999)

18. Bar-Shalom, Y., Li, X.-R.: Multitarget-Multisensor Tracking: Principles and Techniques. YBS Publishing, Storrs, CT (1995)

19. Gustafsson, F.: Statistical Sensor Fusion, 2nd edn. Studentlitteratur, Lund, SWE (2012)
20. Albrektsen, M.S., Johansen, T.A.: User-configurable timing and navigation for UAVs. Sensors **18**(8), 1–27 (2018)

Mika Okuhara received MEng (Hons) in Aerospace System Engineering in 2020 from the University of Glasgow. She is currently working on the Phased Array Radio Navigation System on unmanned aerial vehicles as a PhD candidate at the Department of Engineering Cybernetics, the Norwegian University of Science and Technology (NTNU).

Torleiv H. Bryne received his M.Sc. and PhD in Engineering Cybernetics in 2013 and 2017, respectively, both from the Norwegian University of Science and Technology (NTNU). He has previously been a Research Scientist at SINTEF, Trondheim, Norway, and is currently an Associate Professor at the Department of Engineering Cybernetics, NTNU. His research interests are in the field of estimation applied to navigation and autonomous systems. Unmanned aerial vehicles and marine applications are the main focus areas of his research. He recently co-founded the spin-off company SentiSystems.

Kristoffer Gryte received his MSc and PhD in Engineering Cybernetics in 2015 and 2020, respectively, both from the Norwegian University of Science and Technology (NTNU). He currently works as a researcher on software for autonomous systems at NTNU. His research interests currently revolve around mobile robots, particularly aerial, including guidance, navigation and control.

Tor Arne Johansen received the M.Sc. and Ph.D. degrees in electrical and com-puter engineering from the Norwegian University of Science and Technology (NTNU), Trondheim, Norway, 1989 and 1994, respectively. From 1995 to 1997, he worked with SINTEF, Trondheim, Norway, as a Researcher before he was appointed as an Associated Professor with NTNU in 1997 and Professor in 2001. He has authored or coauthored several hundred arti-cles in the areas of control, estimation, and optimization with applications in the marine, aerospace, automotive, biomedi-cal, and process industries. In 2002, he cofounded the com-pany Marine Cybernetics AS, Trondheim, Norway, where he was the Vice President until 2008. He is currently a Principal Researcher with the Center of Excellence on Autonomous Marine Operations and Systems (NTNU-AMOS), NTNU and Director of the Unmanned Aerial Vehicle Laboratory, NTNU and the Small-Sat Laboratory, NTNU. He recently cofounded the spin-off companies Scout Drone Inspection, Trondheim, Norway; UBIQ Aerospace, Trondheim, Norway; Zeabuz, Trondheim, Norway; and SentiSystems, Trondheim, Norway. Dr. Johansen is the recipient of the 2006 Arch T. Colwell Merit Award of the SAE.